

High-efficiency receiver architecture for resonance-fluorescence and Doppler lidars

John A. Smith^{1,2} and Xinzhao Chu^{1,*}

¹Cooperative Institute for Research in Environmental Sciences & Department of Aerospace Engineering Sciences, University of Colorado Boulder, 216 UCB, CIRES, Boulder, Colorado 80309, USA

²e-mail: John.A.Smith@colorado.edu

*Corresponding author: Xinzhao.Chu@colorado.edu

Received 17 November 2014; revised 20 January 2015; accepted 21 January 2015; posted 25 February 2015 (Doc. ID 226930); published 6 April 2015

A high-efficiency lidar receiver architecture that emphasizes boosting the receiver collection efficiency of resonance-fluorescence and Doppler lidars has opened up new avenues of study for the mesosphere and lower thermosphere-extended (MLT-X) at sites in Boulder, Colorado, USA, and Cerro Pachón, Chile. Described in this work are in-depth considerations in the design, construction, and alignment of Na Doppler lidar receivers that have yielded signal levels typically 5–10 times higher per power-aperture product than any demonstrated in the literature, to these authors' knowledge, making studies of fine-scale MLT turbulence and tenuous thermospheric layers in Na possible with temperature and vertical wind capability for the first time. A lowering of the detection threshold by higher receiver collection efficiency at Cerro Pachón has enabled this Na Doppler lidar to extend its measurement range far higher into the thermosphere, to regions with Na density less than 3 cm^{-3} . With renewed interest in the MLT-X region prompted by recent lidar discoveries of Fe in the thermosphere reaching 170 km at McMurdo, Antarctica, the receiver optimizations we have made now enable addressing an important need in the community. In addition, the higher spatial and temporal resolutions afforded by high signal-to-noise ratio, down to resolutions of $\sim 20 \text{ s}$ and $\sim 20 \text{ m}$, promise to make the first direct measurements of eddy flux in the mesopause region possible. Results from deployment of optimized receivers at the Table Mountain Lidar Observatory in Boulder, the Andes Lidar Observatory at Cerro Pachón, and the Arecibo Observatory in Puerto Rico are presented to demonstrate the power and portability of our methods that are readily applicable to other lidar varieties, including, but not limited to, the newly developed Fe Doppler lidar and recently upgraded K Doppler lidar. © 2015 Optical Society of America

OCIS codes: (010.1080) Active or adaptive optics; (010.3640) Lidar; (220.2740) Geometric optical design; (280.3640) Lidar; (280.7060) Turbulence; (280.6780) Temperature.

<http://dx.doi.org/10.1364/AO.54.003173>

1. Introduction

Future endeavors in studies of the atmosphere and space will require instruments capable of measuring both temperature and wind with unprecedented resolution and coverage. Recent discoveries enabled by the Fe Boltzmann lidar observations at McMurdo, Antarctica, reveal that neutral, unbound Fe layers can extend well into the thermosphere, reaching 170 km or higher [1,2]. Measurements from the Fe

Boltzmann lidar have provided accurate temperatures of the neutral atmosphere and characterized gravity waves from 30 to $\sim 170 \text{ km}$. Following this discovery, faint layers of thermospheric K and Na observed by lidars above 110 km have been reported [3–6]. The extraordinarily large backscatter cross section of atomic absorption and spontaneous emission by meteoric metal atoms such as Fe, Na, and K in the mesosphere and thermosphere enables relatively strong returns from those regions. With an effective cross section 10^{14} times larger than Rayleigh scattering and 10^{17} times higher than Raman scattering, resonance fluorescence excited by resonance-fluorescence

Doppler and Boltzmann lidars from these species in the Earth's middle and upper atmosphere has enabled the earliest studies of the structural evolution of temperature and wind in the mesopause region (75–110 km) (e.g., see work summaries in [7] and [8] and work after 2003 in [9–19], etc.). The discoveries of neutral Fe, K, and Na atoms into previously inaccessible regions of the thermosphere (100–200 km) promise to help address key science topics, such as plasma-neutral atmospheric coupling [1] and dynamics of the space-atmosphere interaction region [20,21]. Like their Rayleigh lidar counterparts, resonance-fluorescence lidars are also capable of measuring temperatures along with tidal and gravity wave signatures in the stratosphere and mesosphere (30–75 km) [22–24]. By introducing the atomic double-edge filter technique, resonance-fluorescence lidar wind measurements can be extended down to 5–50 km [25,26].

With a measurement range that extends from 30 km to almost 200 km, resonance-fluorescence lidars have already been able to make significant contributions to the scientific understanding of vertical energy and momentum transport mechanisms and coupling processes. Ground-based lidars have provided insight into small-scale, transient phenomena which would not have been possible to resolve by radars, balloons, rockets, or satellite-based instruments. Despite these achievements to date, resonance fluorescence lidar has not reached its potential, as indicated by lidar simulations that prescribed far higher signal levels. The Student Training and Atmospheric Research (STAR) Na Doppler lidar constructed by graduate students in our group at the University of Colorado in summer 2010 obtained ~20 photon counts per laser shot through the Na layer from mid-July to mid-September. Although the signal levels varied with the Na column abundance, and had increased up to ~50 counts per shot during a meteor shower, typical values remained at ~20 counts per shot for this lidar equipped with a Cassegrain telescope of 400 mm in diameter and laser power of 450 mW. These signal levels were comparable to other Na Doppler lidars when scaling with the power-aperture product, and the data was still valuable, leading to the first simultaneous observational study of correlations among Na/Fe layers and temperature in the mesopause region [27]. However, lidar simulations for the STAR lidar parameters expected signal levels of at least 200 counts per shot for this 60 mW m² power-aperture product. In order to verify whether the lidar simulations were giving reasonable estimates, we revisited the STAR lidar receiver design and implementation in 2011. Ray-tracing software was employed to model the receiver and the installation of optical components followed the modeled values precisely. Signal levels of ~200 counts per shot were achieved, in accordance with lidar simulations. This exercise indicates that the factor of 5–10 signal deficiency is likely a widespread problem among other resonance-fluorescence lidars in the field.

Our experience advocates for the importance of architecture in the lidar receiver design and implementation. By optimizing receivers, the potential for resonance-fluorescence lidars can be realized fully, opening up new avenues for scientific research. For example, vertical transport of heat and constituents by turbulent eddy mixing has profound effects on the chemistry, composition, and thermal structure of the atmosphere below the turbopause, but this process is poorly characterized due to the lack of high-resolution (seconds and 10's meters) measurements of temperature, vertical wind, and constituent density simultaneously in the mesosphere and lower thermosphere (MLT) [28]. Since the precision of these measurements is shot-noise-limited, large photon fluxes from the mesopause region are required, fluxes that were not thought possible with existing lidars. However, an upgrade to the STAR lidar with an 810 mm diameter telescope along with an efficient receiver design, to be described in this paper, has now achieved signal levels comparable to lidars once operating at Starfire Optical Range and Maui Space Surveillance Complex, which used telescopes of 3.5 m diameter and had 40 times the power-aperture product, but 1/5 photodetector quantum efficiency (8% then versus 40% now) [17], making eddy flux estimation from routine datasets feasible for the first time. Certainly, the high efficiency of the lidar receiver will also help expand the lidar detection range, pushing the detection of tenuous metal layers to even higher altitudes, and many more phenomena will be investigated with unprecedented resolution. Furthermore, the knowledge gained in high-efficiency receiver design will assist the development of the proposed large-aperture lidar observatory, currently under consideration by the Coupling, Energetics and Dynamics of Atmosphere Regions (CEDAR) community [29]. CEDAR is a program primarily sponsored by the National Science Foundation.

2. Architecture of Receiver Design

Saturation of the resonance fluorescence limits the laser power density that can be applied to the MLT metal layers. If power density is reduced through increased beam divergence, then the optical extent of the receiver system must be similarly increased to maintain the collection efficiency. Consequently, saturation places fairly hard limits on lidar transmitter and receiver designs, emphasizing the vital importance of optimizing those systems within these restrictions.

A. Saturation Effects in Resonance-Fluorescence Lidar

Resonance-fluorescence Doppler lidars use narrow-band lasers to excite strong resonance fluorescence from free atoms of Fe, Na, or K metals in the mesopause region (75–115 km). The need to avoid saturation in three-frequency resonance Doppler lidars places constraints on the minimum beam divergence and, therefore, the minimum receiver field of view for efficient collection of backscatter. Scattering from

resonant species, such as Fe, Na and K, is subject to saturation for sufficiently high laser intensity due to the finite lifetime of excited states, causing reduction of ground-state atoms available for absorption. The effect has been studied in potassium [30] and sodium [30–34]. Deriving temperature, wind, and density from resonant atom scattering requires the assumption that backscatter intensity for a given volume is directly proportional to incident laser intensity and the backscatter cross section. For the three-frequency technique, saturation is indistinguishable from warmer temperatures since both produce an apparent broadening of the effective cross section. Although saturation can be estimated in principle, the uncertainty in variables, such as day-to-day lower atmosphere transmission and pulse-to-pulse energy, make saturation estimates unreliable. For three-frequency Doppler lidars, the policy is to avoid nonlinear scattering processes by controlling the laser pulse intensity by adjusting the divergence when necessary.

Saturation is a function of the laser pulse energy, temporal pulse width, radiative lifetime, effective absorption cross section and atomic structure of the metal atoms under study. It is also a function of the spatial distribution of the pulse energy at the altitudes of resonant scattering, which can be controlled by the divergence. Accurate estimate of saturation has to come from detailed calculations using quantum mechanics, and factors like optical pumping and stimulated emission must be considered for different cases of laser pulse duration and spectral linewidth [7]. To provide a rough estimate of saturation for different metal species in this study, we use a two-level energy structure model, following Megie *et al.* [30], Welsh and Gardner [31], and Chu and Papen [7]. Equation (1) defines the time scale for stimulated emission τ_s , with the ratio of this time scale to the natural lifetime τ_N indicating the degree of saturation [30]:

$$\tau_s = \frac{z^2 \Omega \Delta t_L}{2 \sigma_{\text{eff}} N_L T_a} = \frac{(hc/\lambda)}{2 I_{\text{MLT}} \sigma_{\text{eff}}}$$

$$\Omega = \pi \theta_{1/2}^2$$

$$I_{\text{MLT}} = [P_L/A]_{\text{MLT}}, \quad (1)$$

where z is the altitude of the metal layer; Ω is the solid angle illuminated by the laser beam, determined by the beam divergence half-angle $\theta_{1/2}$; Δt_L

is the full width at half-maximum (FWHM) of the laser pulse duration; σ_{eff} is the effective scattering cross section of the metal atom; N_L is the total number of photons in each laser pulse; and T_a is the one-way transmission of the lower atmosphere. Here, h is the Planck constant, c is the light speed, λ is the laser wavelength, and I_{MLT} is the laser intensity, or power per unit area, at the base of the metal layer. This simple model ignores optical pumping effects and assumes that the spectral width of the laser pulse is large compared to the natural linewidth; therefore, it cannot provide a precise account of the saturation effect for all metals. However, the approximation is quite accurate for the $\alpha^5 D_4 - z^5 F_5^0$ transition at 372 nm in the major Fe isotopes due to the lack of hyperfine levels. Optical pumping is less important for the short pulse width lasers of suitable Na transmitters [7], so the approximation holds reasonably well for Na lidars as well. Some values of the time scale for stimulated emission are tabulated in Table 1 using typical transmitter properties for each respective wavelength along with natural radiative lifetimes.

We use the ratio of this time scale τ_s to the natural lifetime τ_N as a proxy for the saturation, where greater values of the ratio τ_s/τ_N indicate less saturation. Sodium (Na) and potassium (K) suffer from higher saturation due to their higher absorption cross sections and possibilities of optical pump issues, but the scarcity of potassium compared to Na means that higher powers are required to reach sufficient signal levels, introducing more saturation. In addition, only Si avalanche photodiodes (APDs) have quantum efficiencies at 770 nm comparable to the large-active-area photomultiplier tubes (PMTs) commercially available at the Na line 589 nm and the Fe lines 372 nm/386 nm. The far smaller active area of Geiger mode APDs, though possessing superior quantum efficiency at 770 nm, place stringent limits on the maximum beam divergence for 770 nm, which will be demonstrated in Section 2.C, Eq. (13). Having a smaller allowable beam divergence combined with the higher required power makes saturation of K a limitation to K Doppler lidar performance potential.

With a similar cross section, but an abundance of more than 80 times that of potassium, Na requires less power to achieve the same performance. In addition, large-active-area PMTs of 40% quantum efficiency are now readily available, making large

Table 1. Rough Estimate of Metal Layer Saturation for Current Resonance Doppler Lidars^a

Metal/line (nm)	Δt_{FWHM} (ns)	$\theta_{1/2}$ (μrad)	E_p (mJ)	T_a	σ_{eff} (200 K)	τ_s (μs)	τ_N (ns)	τ_s/τ_N
Na/589	10	500	16	0.7	$15 \cdot 10^{-16} \text{ m}^2$	0.64	16	~ 40
K/770	200	250	115	0.8	$13 \cdot 10^{-16} \text{ m}^2$	0.34	27	~ 13
Fe/372	250	125	43	0.5	$0.9 \cdot 10^{-16} \text{ m}^2$	13.7	62	~ 221
Fe/386	250	125	43	0.6	$0.4 \cdot 10^{-16} \text{ m}^2$	24.8	103	~ 241

^aHere, higher values of s/N indicate less saturation. Current resonance Doppler lidars are compared on the basis of their metal's respective ease of saturation. A flashlamp-pumped-Nd:YAG-based laser transmitter was assumed for the 589 nm source and a ring Alexandrite-based laser for the 770, 372 and 386 nm sources. Here, E_p is the single laser pulse energy and σ_{eff} is the approximate peak cross-section at temperature of 200 K.

beam divergences possible. However, the significantly shorter temporal pulse width of suitable, high pulse energy 589 nm sources for Na based on Nd:YAG laser pumps, compared to low-gain, long pulse width Alexandrite ($\text{Cr}^{3+}:\text{BeAl}_2\text{O}_4$) laser transmitters in Fe, makes saturation only avoidable at relatively large beam divergences [7].

The availability of transmitters with sufficiently long pulse widths, or detectors with sufficiently high quantum efficiencies and large active areas in combination with the natural properties of the metal under study all factor into the receiver design, providing the starting point for the Na, Fe, or K Doppler lidar receiver design process.

B. Geometric Overlap in Biaxial Lidars

Resonance-fluorescence Doppler lidars excite strong resonant scattering from unbound Fe, Na, or K metals in the MLT at, typically, three unique frequencies distributed about the Doppler absorption line shape to infer both wind and temperature. Simultaneously, most resonance lidars require scattering from the so-called “Rayleigh” altitudes at 30–75 km to normalize the resonance signal against variations in the transmitter pulse energy and transmission of the lower atmosphere [7]. Meanwhile, the beam’s divergence must be large enough to avoid fluorescence saturation from the metal layers in question, which would otherwise add uncertainty to temperature, density, and wind retrieval (Section 2.A).

The range of the MLT region from ground-based platforms combined with the wide receiver field of view needed to accommodate the beam divergence requires that the transmitter pulse energy be relatively large in order to compete with background noise. Large pulse energies, in turn, produce intense scattering from the near field by aerosol and Rayleigh scattering, which must be blocked to prevent detector damage and nonlinearities, such as signal-induced, or “sloped,” background. In resonance Doppler lidars, selective blocking of low altitudes is accomplished either by extending the transmitter-receiver separation, typically by 1–3 m, or use of an optical chopper [7]. Sometimes a combination of the two is employed to provide better isolation between the transmitter and receiver. Gating circuits that can rapidly switch the high voltage to one or more dynodes of the PMT have been employed in Rayleigh lidars to further suppress signal-induced background effects [35], though response after the gating can be difficult to characterize due to transient effects of the switching [36]. By increasing the transmitter-receiver separation and by pushing the complete geometric overlap further afield, however, there is a risk that the relative geometric overlap between the Rayleigh and resonance altitudes will become sensitive to unavoidable errors in the beam pointing.

To see what effect the errors in beam pointing have on the geometric overlap, we introduce the exaggerated geometry of Fig. 1. Here, the optical axis of the telescope and that of the beam are separated by a

nonzero distance L so that nearer ranges are separated by distinct field angles that can be blocked by a field stop. The beam divergence is defined as the full angle corresponding to where the beam intensity decreases to $1/e^2$ of the peak intensity. If a Gaussian laser beam is assumed, an angular integration of 4 times the beam divergence half-angle $\theta_{1/2} (@I_0/e^2)$ encompasses more than 99% of the energy in the beam while an angular beam width of 2 times the divergence half-angle includes 86.5% of the energy. Regardless of the separation, since the signal from the resonance layer is maximized by way of the beam steering, the axes of the transmitter and receiver always intersect at a range R , often corresponding to the altitude at which the signal is maximized. The range $r_{1/2}$ at which the geometric overlap reaches one half of its maximum and the range r_0 at which the overlap is small ($<1\%$) are functions of the field of view θ_{FOV} , beam divergence half-angle $\theta_{1/2}$, the transmitter-receiver separation L , and the range R to the aligned altitude, as given in Eq. (2):

$$r_{1/2} \approx \frac{L}{\theta_{\text{FOV}}/2 + L/R}, \quad r_0 \approx \frac{L}{\theta_{\text{FOV}}/2 + L/R + 2\theta_{1/2}}. \quad (2)$$

As the separation is increased, however, useful ranges are pushed out to field angles that lie closer to the edge of the field stop. Pointing errors can then substantially alter the relative geometric overlap between, for example, the Rayleigh and resonance altitudes in resonance lidars. Figure 2 shows a

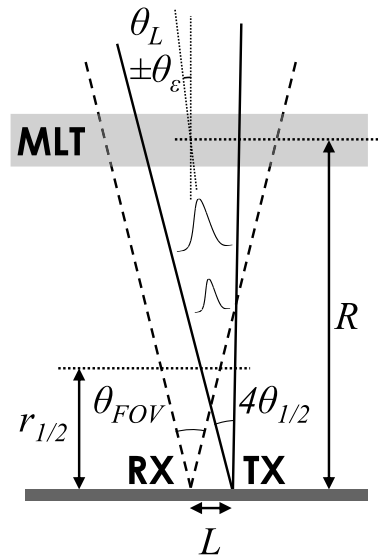


Fig. 1. Lidar geometry diagram (not to scale) illustrates the geometric overlap between receiver (RX) and transmitter (TX). Rays indicating the RX field of view and TX divergence are indicated alongside each other for a zenith-pointing telescope and a nonzero transmitter-receiver separation L . A full angle divergence of 4 times the half-angle divergence $\theta_{1/2}$ is assumed, which encompasses more than 98% of the energy in the beam. In practice, the signal from the resonance at the MLT altitude R is maximized. In this case, the axes of the transmitter beam and field-of-view intersect at the MLT, as shown.

ZEMAX-computed geometric overlap function $G(r)$ for a receiver with a field of view matched closely to the beam divergence for various separations of the transmitter and receiver and using values that are typical of those from Na Doppler lidars at Cerro Pachón, Chile, and Boulder, Colorado.

For Gaussian or Gaussian-like beams, a close analytical approximation to the geometric overlap can be found through one-dimensional integration with upper and lower bounds set by the receiver field-of-view [Eq. (3)]:

$$S(r) = \frac{2L}{\theta_{1/2}} (1/R - 1/r), \quad A = \theta_{\text{FOV}}/\theta_{1/2}$$

$$G(r) \approx \frac{1}{2} (\text{erf}(S(r) + A) - \text{erf}(S(r) - A))$$

$$\text{erf}(x) \equiv \frac{2}{\sqrt{\pi}} \int_0^x e^{-t^2} dt. \quad (3)$$

Although nearly complete overlap is attained at 40 km for all three separations indicated in Fig. 2, Fig. 3 shows the degree to which larger separations can produce normalization errors in resonance lidar which are more sensitive to the pointing error. From the expression given for the geometric overlap, we can also express the sensitivity of the geometric overlap at range r_* to a pointing error θ_ϵ analytically:

$$\frac{dG(r_*)}{d\theta_\epsilon} = \frac{2}{\theta_{1/2}\sqrt{\pi}} (\exp(-(S(r_*) + A)^2) - \exp(-(S(r_*) - A)^2)). \quad (4)$$

Geometric overlap can be exploited to reduce the collected near-field signal, but the sensitivity of the geometric overlap to pointing errors that can impact density measurements, will increase the further afield the overlap is pushed.

C. Optical Extent Matching in Lidar Receivers

The telescope defines the minimum optical extent, area-solid angle product ($A\Omega$), or étendue of the

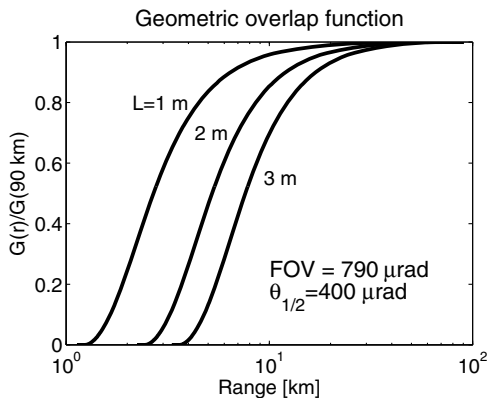


Fig. 2. Geometric overlap functions computed using ZEMAX for a field of view (FOV) of 790 μrad and half-angle beam divergence ($\theta_{1/2}$) of 400 μrad and for three values of the different transmitter-receiver axis separations L .

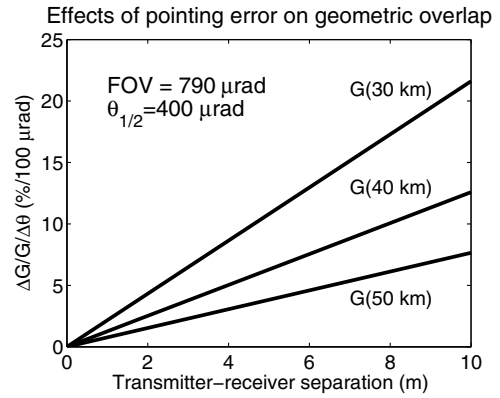


Fig. 3. Beam pointing/beam steering errors are more severe for larger transmitter-receiver separations, requiring higher normalization altitudes to limit the normalization errors for larger separations.

collected light. The minimum optical extent remains a constant through a lossless receiver system as required by the principle of optical invariance. Both the Boulder and Cerro Pachón lidars employ fiber-coupled, prime focus telescopes, wherein a large core (1000–1500 μm) fiber is positioned at the focal plane of a Newtonian primary. Resonance Doppler lidars employ fibers for several reasons—ease of isolating the telescope from the transmitter, scrambling of the field angle-range dependence, and ease of relaying signal to the receiver optics. Scrambling prevents field angles from mapping to different regions of illumination across varying sensitive regions of the detector’s active area. The fiber is routed to a postfiber, consisting of a collimating lens, an interference filter and the detector, often with a condensing lens. When the fiber is “matched” to the telescope, the following relationships between the parameters of the telescope and that of the fiber are satisfied when vignette and fiber apodization effects are ignored:

$$\begin{aligned} [A\Omega]_{\text{telescope}} &= [A\Omega]_{\text{fiber}} \\ [A\Omega]_{\text{telescope}} &\sim (\pi(D_{\text{primary}}/2)^2)(\pi\theta_{\text{FOV}/2}^2) \\ [A\Omega]_{\text{fiber}} &\sim (\pi(D_{\text{core}}/2)^2)(\pi\text{NA}^2) \\ \frac{D_{\text{primary}}}{D_{\text{core}}} &\cong \frac{\text{NA}}{\theta_{\text{FOV}/2}} \\ \text{NA} &\cong \frac{1}{2(f/\#)}, \end{aligned} \quad (5)$$

where $\theta_{\text{FOV}/2}$ is the field-of-view half-angle (radians), NA is the numerical aperture, D_{core} and D_{primary} are the diameters of the fiber core and primary mirror, respectively, and $f/\#$ is the f -number of the telescope (f/D_{primary}). In order to avoid losses from bends along the length of the fiber, the numerical aperture used above should equal the effective NA [37]:

$$\text{NA}_{\text{effective}} = \left(\text{NA}^2 - \frac{2a}{R} n^2 \right)^{1/2}, \quad (6)$$

where a is the core radius, n is the core index of refraction, and R is the bend radius. For a 1000 μm silica core fiber of $\text{NA} = 0.22$ with a 0.5 m bend radius, the effective numerical aperture is reduced by approximately 5%-6%.

If light from this fiber, after collimation, uniformly illuminates an interference filter of diameter D_{filter} , the diverging cone of ray angles incident on the face of the filter will have a divergence half-angle $\theta_{1/2}$ of

$$\theta_{1/2} = \frac{D_{\text{core}}}{D_{\text{filter}}} \text{NA}. \quad (7)$$

Each ray experiences a filter transmission function in which the center wavelength is shifted as a function of the incident ray angle. To determine the transmission of the filter for an arbitrary divergence half-angle $\theta_{1/2}$ we integrate the filter line shape $f(\lambda)$ over the range of angles defined by the optical extent [38]

$$T(\lambda_0) = \frac{1}{\lambda(\theta_{1/2}) - \lambda_0} \int_{\lambda_0}^{\lambda(\theta_{1/2})} f(\lambda) d\lambda, \quad (8)$$

where λ_0 is the unshifted center wavelength of the filter and $\lambda(\theta_{1/2})$ is the center wavelength corresponding to the maximum incident angle. For an interference filter with a Lorentzian-like line shape and small divergence angles, the integral evaluates to

$$T(\lambda_0)/T_0 = (1/S^2) \arctan(S^2) \\ S = \left(\frac{\theta_{1/2}}{n_*}\right) \sqrt{\frac{\lambda_0}{\Delta\lambda_{\text{FWHM}}}}, \quad (9)$$

where T_0 is the peak transmission of the filter at normal incidence, $\Delta\lambda_{\text{FWHM}}$ is the FWHM bandwidth of the filter, n_* is the effective index of refraction of the filter, and we have made use of relation Eq. (10) to convert the half-angle to a shift in center wavelength,

$$\lambda = \lambda_0 \sqrt{1 - \left(\frac{1}{n_*} \sin \theta_{1/2}\right)^2} \sim \lambda_0 \left(1 - \frac{1}{2} \left(\frac{1}{n_*}\right)^2 \theta_{1/2}^2\right). \quad (10)$$

Relation Eq. (9) is valid for both interference filters and Fabry-Perot interferometers. Values of S of less than $\sim 1/2$ result in negligible transmission loss ($< 2\%$). Substituting $S = 1/2$ into Eq. (9) and solving for the corresponding solid angle results in an optical extent for the circular interference filter, or Fabry-Perot interferometer, of approximately

$$[\text{A}\Omega]_{\text{filter}} \sim \frac{\pi^2}{16} n_*^2 \left(\frac{\Delta\lambda_{\text{FWHM}}}{\lambda_0}\right) D_{\text{filter}}^2. \quad (11)$$

The filter's effective index of refraction (n_*) is a parameter usually specified by the manufacturer and the divergence half-angle $\theta_{1/2}$ is as defined in Eq. (7). Figure 4 illustrates the dependence of transmission on the half-angle for typical values of the ratio $\lambda_0/\Delta\lambda_{\text{FWHM}}$ and the effective index.

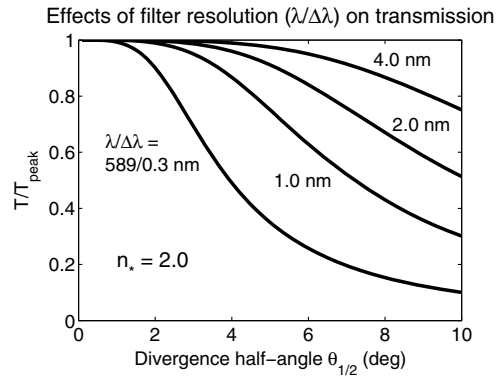


Fig. 4. Filter resolution influences the sensitivity of the filter to diverging/converging beams, the half-angle of which is limited by the optical extent defined by the telescope and the filter diameter.

The presence of apertures also limits the maximum optical extent of a receiver. This can be a limitation in Faraday anomalous dispersion optical daytime filters [7], which require two small Glan-Taylor polarizers positioned about a large heated cell in a uniform magnetic field (Fig. 5). The optical extent of two coaxial apertures of area A_1 and A_2 separated a distance L is given by Eq. (12):

$$[\text{A}\Omega]_{2\text{-aperture}} = \frac{A_1 A_2}{L^2}, \quad \text{when } L^2 \gg A_1, \quad L^2 \gg A_2. \quad (12)$$

This limitation could also apply to a window and photocathode comprising a photomultiplier tube, or the small limiting aperture of an avalanche photodiode's active area. In the latter case, we may assume that the numerical aperture approaches its limit, corresponding to a solid angle of 2π for a planar detector. The minimum spot size with diameter D_{min} that any optical system can focus the light from a telescope with diameter D_{primary} and field-of-view half-angle $\theta_{\text{FOV}/2}$ is given by Eq. (13):

$$D_{\text{min}} = \frac{D_{\text{primary}} \theta_{\text{FOV}/2}}{\sqrt{2}}. \quad (13)$$

The lowest of the optical extent quantities defined above limits the allowable optical extent of the telescope for efficient light collection.

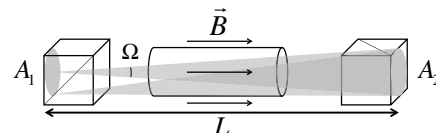


Fig. 5. Essential arrangement of the Na Faraday anomalous dispersion optical filters (FADOF) used for daytime background filtering in Na Doppler lidar. A heated Na cell in a strong magnetic field \vec{B} is positioned between two Glan-Taylor polarizers. Only a narrow band of light (~ 2 GHz) near the D_{2a} line of Na experiences a strong Faraday rotation effect and, subsequently, a minimum extinction from the second, crossed polarizer.

3. Architecture of Receiver Implementation

The practical design considerations in Section 2 cover the majority of resonance lidar receiver configurations, but aberrations complicate further theoretical treatment of the optical design. To ensure efficient light collection, we have employed ray-tracing software (ZEMAX) to ensure that light is efficiently relayed to the photodetector. Methods of positioning the fiber and other optics in the prefiber and postfiber receivers are addressed in this section also.

A. Impact of Aberrations on Prefiber Coupling Efficiency

For perfect imaging, a fiber that has an optical extent matched to the telescope is sufficient. However, aberrations will also impact the performance of the receiver. Coma presents in objects off the optical axis of parabolic Newtonian primary mirrors, causing a fiber that is horizontally (x, y) shifted sufficiently far from the optical axis of the telescope to experience degraded coupling efficiency. Defocus is particularly damaging to coupling efficiency. The effects of both

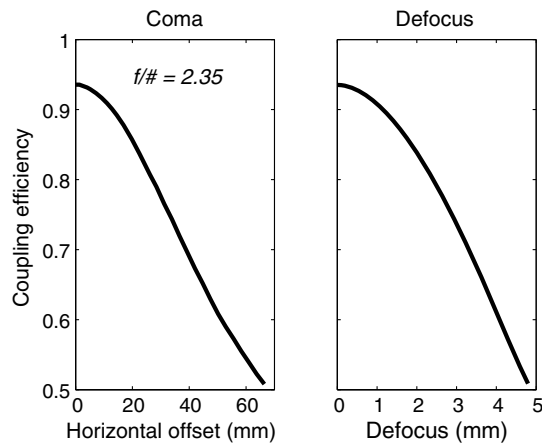


Fig. 6. Effects on fiber coupling efficiency of coma (left) and defocus (left) of the positioning error of the fiber about the focal point of the telescope.

coma and defocus are illustrated in Fig. 6. Positioning errors of a few millimeters are sufficient to greatly degrade fiber coupling efficiency. For example, the coupling efficiency of an $f/2.35$ telescope typical of Na Doppler lidar receivers will drop in half for a 5 mm defocus, or a horizontal offset of less than one tenth the primary diameter.

B. Finding Telescope Focus and Optical Center

We have developed a method of aligning prefibers which uses a camera to ensure that the fiber coupling efficiency is maximized. Adjusting receiver optics by maximizing the lidar signal is not always reliable due to the shot-noise-limited nature of resonance-fluorescence signal levels, which can also vary with time, and the number of adjustments involved. Instead, for a zenith-pointing telescope, the approximate focal point can be located by two commercially available laser levelers with nadir beams located diametrically opposite one another above the primary mirror, similar to methods employed by others [39,40]. The intersection of these beams after reflection from the primary with a string plummet aligned to the mechanical center of the primary mirror locates the approximate focal point (Fig. 7). To locate the precise focal point, the laser levelers are removed and a camera (e.g., Thorlabs DCC1545M) is installed at the approximate focal point to observe the star field at night. Coma from stars at the focus will be apparent in the images and will point to the optical center. An offset of 1 mm or 0.5 mrad from the optical axis of the primary along the focal plane of the telescope will produce very noticeable coma for $f/2.35$, 810 mm primaries. Once coma and defocus are minimized for a star crossing the center of the sensor using the x, y , and z adjusters, the focal point and field center are now located relative to a flange and the fiber can then be installed in place of the camera sensor on the same flange (Fig. 7). In addition to aligning the fiber to the primary, the camera can be used to adjust the pointing of the telescope in zenith and azimuth. Comparing the star field observed by the camera to

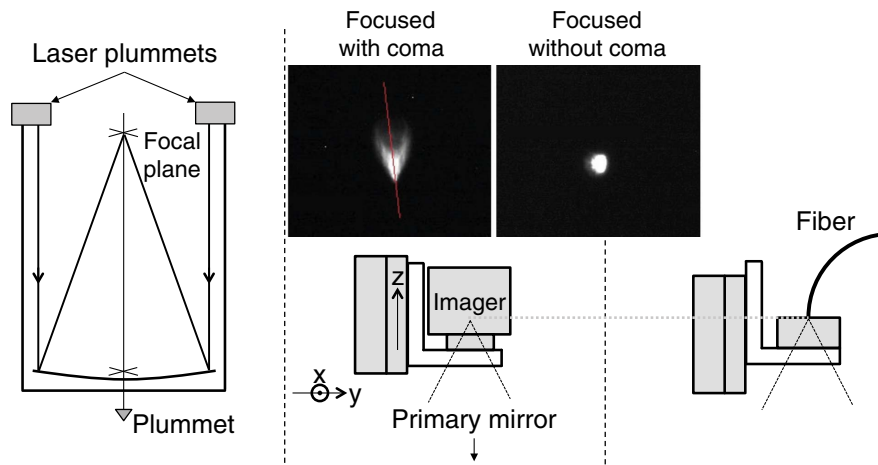


Fig. 7. Alignment of prefiber involves use of laser plummets for coarse alignment and a camera for fine positioning. Coma like that in the left image would be evident approximately 5 mm from the optical center.

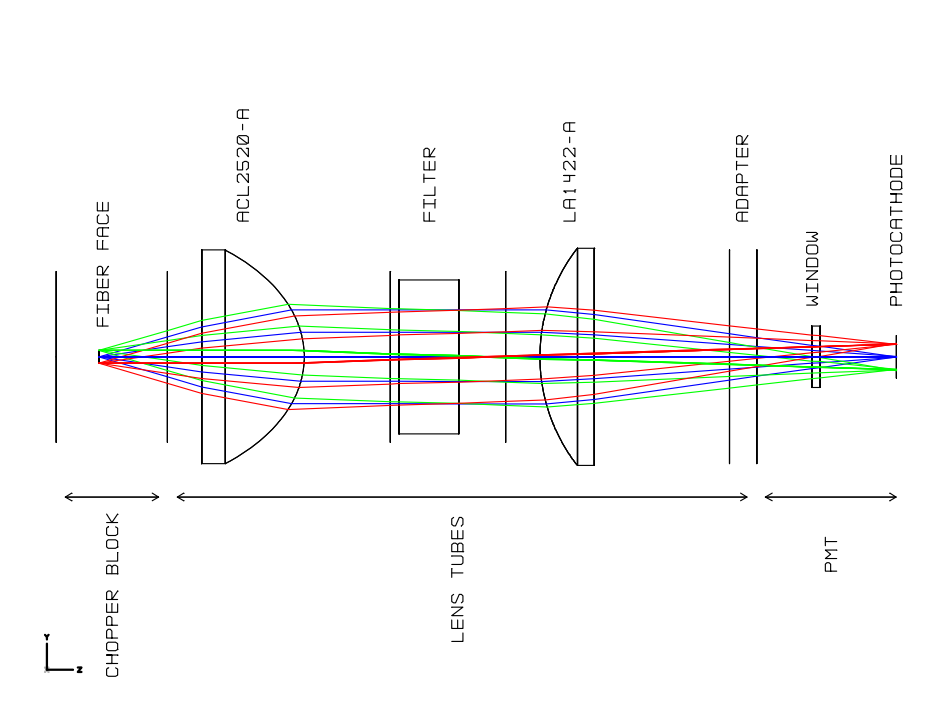


Fig. 8. Postfiber designed in ZEMAX showing parts and positions of optical elements in the system. The fiber has a 1500 μm core with 0.37 numerical aperture. Part number ACL2520-A is a Thorlabs, molded, plano-convex asphere with $f = 20$ mm, $\text{Ø}25$ mm. Part number LA1422-A is a Thorlabs, $f = 40$ mm, $\text{Ø}25$ mm plano-convex spherical lens. The PMT is a Hamamatsu H7421P-40 photon counting head.

a software program (e.g., Stellarium [41]) set to the desired coordinates, small corrections to the telescope's zenith and azimuth can be made. The absolute pointing error is a function of the point spread function, which is typically 100–200 μm in diameter for $f/2.35$ parabolic mirrors, corresponding to an angular pointing error of ~ 50 –100 μrad . After the fiber is installed at the focal point and field center, the fiber tilt can be checked by coupling laser light into the post-fiber end and viewing the scattered illumination on the primary mirror surface. For an underfilled input condition, the fiber output typically exhibits a small divergence and can therefore be used to make precise adjustments to the pointing of the fiber on the primary. This straightforward and robust alignment procedure has been used to precisely align both Newtonian and Cassegrain telescopes for various resonance lidar receivers.

C. Postfiber Alignment

There are numerous variables involved in the alignment and positioning of the postfiber system. Our experience recommends converting the arrangement of lenses, filters, and detector of the postfiber optics in the ray-tracing model to a physical system by eliminating certain alignment variables through directly measuring the relative positions of elements in the system. For Na Doppler nighttime channels at Boulder, Colorado, and Cerro Pachón, Chile, we have a ZEMAX-designed postfiber which includes, in the design, a molded glass aspheric lens for collimation, a Materion–Barr interference filter with 1.0 nm bandwidth, and a condensing lens to efficiently relay

light through the photomultiplier's window and onto the photocathode (Fig. 8).

We have used lens tubes for our receiver systems, which ensure correct alignment of lenses and filters in the system by fixing the optics normal to, and coaxial with, the optical axis. Light tightness is an additional benefit. Calipers are then used to ensure the correct positions of each optic within the tube and relative to each element. Afterward, the camera can

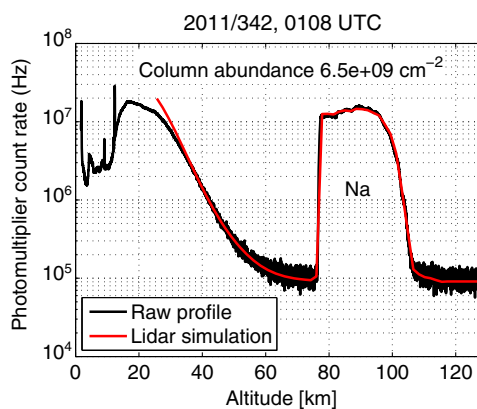


Fig. 9. Lidar simulations are consistent with the raw data obtained for a Na Doppler lidar at Boulder, Colorado, and only diverge in the nearer ranges due to the reduced geometric overlap for this profile at those altitudes. We used 70% for the one-way atmospheric transmission and temperature data was obtained from NRL MSISE-00. The backscatter coefficient of air was computed from [42]. The background level is higher than normal due to the large field of view employed on this night when the PMT and interference filter were mounted directly above the primary.

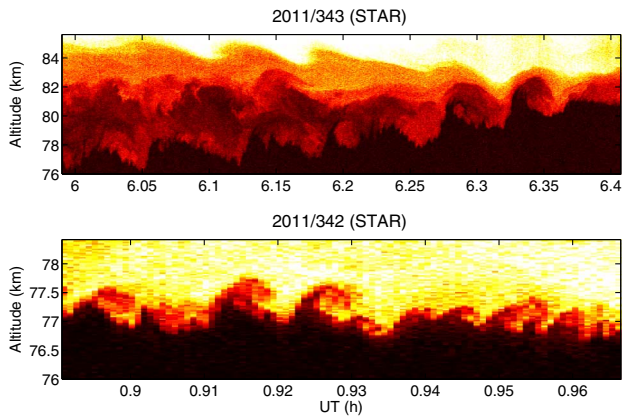


Fig. 10. Turbulence features of the order of 20 s and 24 m in scale are clearly visible on the bottomside of the layer, where the density gradient is large on these nights in December 2011. Data was taken with the STAR Na Doppler lidar, which has a power-aperture product of 0.25 W m^2 .

be threaded onto the detector flange to verify that the light emitted from the fiber end face will be centered on the photocathode and matches the expected size of the spot based on the ray-trace model after propagating through the system. All of the postfiber receiver systems described to this point have been constructed using lens tubes and this method.

4. Case Studies at Boulder, Colorado; Cerro Pachón, Chile; and Arecibo, Puerto Rico

In many cases, applying the techniques described above has yielded signal levels at 4-5 times higher than what any Na Doppler lidar has realized previously. The signal levels that have been obtained are consistent with lidar simulations for a Na Doppler lidar situated at Boulder, Colorado (Fig. 9). The following example cases at three different sites show the effectiveness of the procedure. These improvements have not only enhanced the spatial and temporal resolution of our data, but also lowered the detection threshold for layers as sparse as 2-3 atoms per cubic centimeter in the thermosphere given the current background light levels.

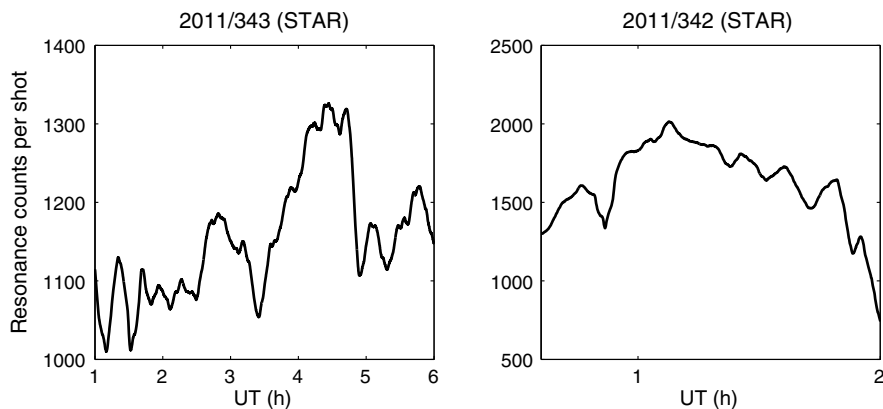


Fig. 11. Resonance Na counts per shot (smoothed) through the whole layer for two nights of data. The power-aperture product for the STAR Na Doppler lidar on these days was approximately 0.25 W m^2 .

To demonstrate resolution improvements, we show profiles of the density at the bottomside of the main layer where there is often a sharp gradient in the sodium abundance and in which turbulence in this region produces features that can be easily resolved in certain nights of data (Fig. 10). The total photon counts per laser shot through the main layers of the metal atoms are often used in the resonance-fluorescence lidar field as an indicator of the lidar signal strength. Despite a small power-aperture product (0.25 W m^2), the STAR Na Doppler lidar at Boulder easily achieves higher than 1000 counts per shot on a regular basis. Figure 11 shows the signal levels for the same two nights in Fig. 10, which reach as high as 2000 counts per shot in December. It is speculated that, due to the high resolution of this data, the profiling of vertical eddy fluxes in the MLT region should be possible (private communication, Chester. S. Gardner, University of Illinois at Urbana-Champaign).

In addition to making the main layer resolvable, higher signal levels enable the lidar to profile exceptionally sparse layers further up into the thermosphere. Several nights of data were taken at Cerro Pachón, Chile, between May 24–30, 2014, in which a sparse layer of sodium was evident in the thermosphere, which only occurred or was only detectable at certain periods (Fig. 12), but was visible during most nights of that campaign. The discovery of these Na layers complements the discovery of thermospheric Fe layers in 2011 [1] and was an unanticipated result of the optimization that will enable greatly expanded observations of the MLT-X region. We also acknowledge the qualitative work by Höffner and Friedman [43] regarding performance optimization and detection linearity of the systems at Kühlungsborn and Arecibo that enabled these lidars to observe metal atoms in the lower thermosphere.

For comparison, we present a typical profile from before and after the receiver optimization steps taken in this work for the Boulder, Colorado, site and the Cerro Pachón, Chile, site (Fig. 13). We also achieved a factor of 4 improvement in signal from the broadband Na resonance-fluorescence lidar

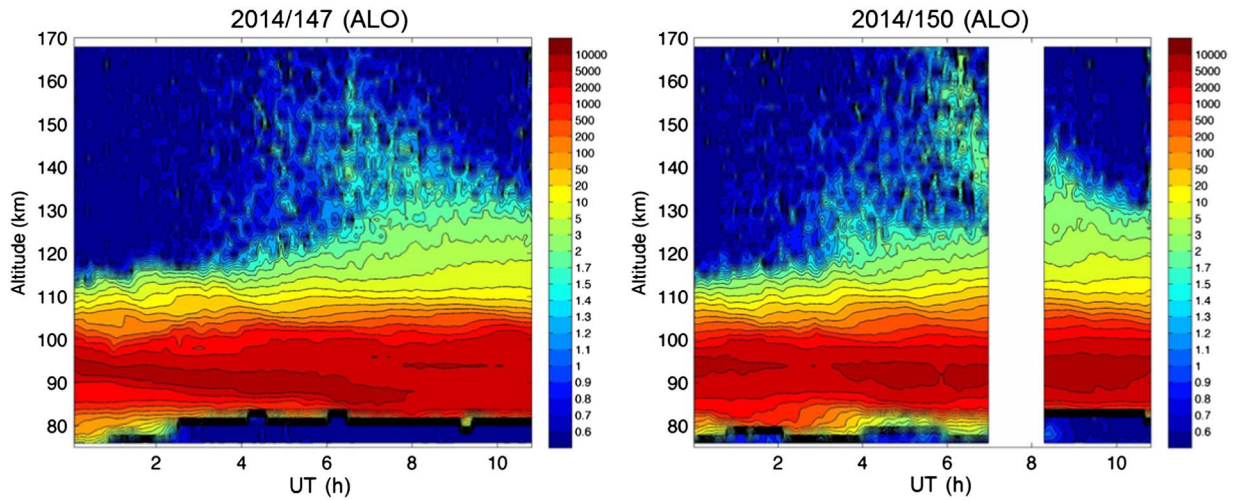


Fig. 12. Thermospheric Na is visible up to nearly 170 km in this smoothed range-time image obtained at Cerro Pachón, Chile, with the University of Illinois Na Doppler lidar. The density of sodium above the main layer (75–115 km) decays exponentially in the thermosphere. Lowering the detection threshold by a factor of 5, our methods have extended the measurement range an additional 50 km, to where the sodium density falls to just 2–3 cm^{-3} . (Figure courtesy Dr. Alan Z. Liu, Embry-Riddle Aeronautical University.)

system at Arecibo Observatory (Fig. 14) predominantly through prefiber and telescope alignment.

In addition, such receiver techniques have been applied to the newly developed three-frequency Major Research Instrumentation Fe Doppler lidar [44–46] at Boulder, Colorado. Even with ~ 1.2 W of power at 372 nm, which is only 1/5 of the designed capability, we have achieved signal levels of ~ 200 – 350 photon counts per laser shot through the Fe layer in September and October 2014. These results match the lidar simulations quite well [44], which predict ~ 1000 counts per shot for 6 W Fe lidar power at a nominal Fe column abundance of $10 \times 10^9 \text{ cm}^{-2}$. We have also applied the receiver techniques to the K Doppler lidar at Arecibo Observatory [16], and achieved a factor of 2 improvement, mainly due to the prefiber and telescope alignment.

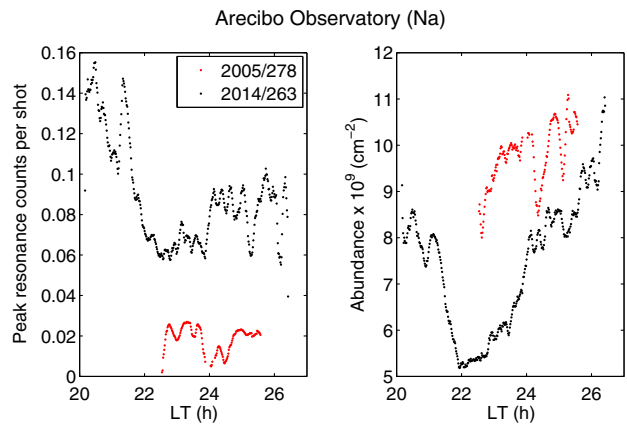


Fig. 14. Comparisons of data before and after receiver optimization at Arecibo Observatory's Na resonance lidar system (photon counts per laser shot per range bin) are shown along with the corresponding column abundance for that evening. Despite a slightly lower abundance, the optimized receiver shows a factor of 4 improvement in signal. (Figure courtesy Dr. Shikha Raizada, Arecibo Observatory.)

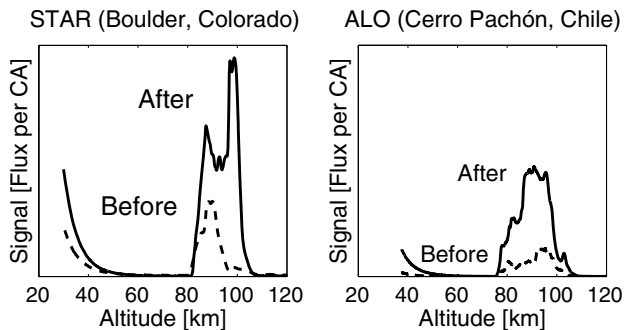


Fig. 13. Comparisons are shown of typical profiles before and after receiver optimization has taken place. Both lidars experienced an improvement of a factor of 3–5 in signal with negligible increase in background. Since these profiles were obtained in different seasons, the signal is roughly scaled by the column abundance for each season. The vertical scale is proportional to the count rate/flux scaled by the column abundance (CA).

5. Conclusions

The lidar receiver architecture presented in this study and deployed to the receiver systems of several resonance-fluorescence and Doppler lidars distributed worldwide has shown a widespread improvement in the obtainable signal levels. The architecture starts with theoretical considerations of key factors involved in the resonance Doppler lidars, including metal layer saturation, geometric overlap between the receiver field of view and the transmitter beam divergence, and matching of the optical extent through the receiver from the telescope to the photodetector. A ray-tracing model is then developed with ZEMAX software to maximize the optical collection efficiency of the receiver for each lidar system. Various procedures have been developed for implementing the

optical modeling to real receiver systems. Our telescope alignment and collimation procedure ensures that the coupling losses due to fiber misalignment are minimized. Considerations in the optical extent, and limiting vignette and apodization losses by matching of the optical extent through the system, have contributed to the dramatic improvements we have observed in these systems. The Eq. (9) we present which predicts the transmission for various values of divergence/convergence half-angle has been shown to be accurate when compared with manufacturer specifications and could be helpful for any design involving interference filters and Fabry-Perot interferometers. Proper implementation of optical modeling, with understanding of the functions of various components and inclusion of fields that represent the full input aperture, is shown to be a powerful tool for the analysis of prefiber and postfiber designs.

The high signal-to-noise ratio afforded by the high-efficiency receiver architecture, a first for resonance Doppler lidars capable of measuring wind and temperature, has opened up new avenues of study for the MLT-X. Boosted lidar signal levels, typically 5–10 times higher than any demonstrated in literature for the same power-aperture product, to these authors' knowledge, have made studies of fine-scale turbulence in the MLT and tenuous thermospheric Na layers possible for the first time with temperature and wind capability. Results by Pfrommer *et al.* [47] demonstrated comparable resolutions, but with many times the power-aperture product of the lidars investigated in this work and, being a broadband system, without temperature/wind capability. With renewed interest in the MLT-X region prompted by recent discoveries of Fe in the thermosphere reaching over 170 km at McMurdo, Antarctica, the receiver architecture optimizations we have made, by making possible the probing of the neutral atmosphere above 100 km, are now addressing an important need for atmospheric and space science research. In addition, the higher spatial and temporal resolutions resulting from the high signal-to-noise ratio promise to make the first direct measurements of eddy flux in the mesopause region possible. This high-efficiency lidar receiver architecture will assist in the development of the Observatory for Atmosphere-Space Interaction Studies (OASIS) and the development of the very large-aperture high-power lidar as the first step toward OASIS, proposed by the CEDAR community. A large-aperture observatory like OASIS, in combination with the receiver design considerations introduced in this work, will enable significantly enhanced coverage of the space-atmosphere interaction region.

We sincerely acknowledge Weichun Fong and Wentao Huang for their contributions to the development and operation of STAR Na Doppler lidar at the Table Mountain Lidar Observatory in Boulder and their assistance in many tests of the receiver implementation worldwide. We wish to acknowledge the contributions of past and present group members

including Ian Barry, Cao Chen, Ian Dahlke, Weichun Fong, Aaron Holt, Wentao Huang, Brendan Roberts, Zhibin Yu, and Jian Zhao. We wish to acknowledge Alan Liu and Tony Mangogna for providing the ALO Na Doppler lidar data from the nights of May 2014 and Shikha Raizada for providing the Arecibo Observatory Na resonance lidar data from October 5th, 2005 and September 20th, 2014. This work was supported by the National Science Foundation grants MRI-0723229, AGS-1136272, and AGS-1115224. John A. Smith sincerely acknowledges the generous support of the NASA Earth and Space Science Fellowship (NESSF) with NASA grant NNX09AO35H and of the CIRES Graduate Student Research Fellowship (GSRF).

References

1. X. Chu, Z. Yu, C. S. Gardner, C. Chen, and W. Fong, "Lidar observations of neutral Fe layers and fast gravity waves in the thermosphere (110–155 km) at McMurdo (77.8°S, 166.7°E), Antarctica," *Geophys. Res. Lett.* **38**, L23807 (2011).
2. X. Chu, Z. Yu, W. Fong, C. Chen, B. Roberts, W. Huang, X. Lu, T. Fuller-Rowell, C. Gardner, A. McDonald, and S. Vadas, "LIDAR observations of thermospheric Fe layers, temperatures and gravity waves at McMurdo, Antarctica," in *Coupling, Energetics and Dynamics of Atmospheric Regions (CEDAR) workshop*, Boulder, Colorado, 2013.
3. J. S. Friedman, X. Chu, C. G. M. Brum, and X. Lu, "Observation of a thermospheric descending layer of neutral K over Arecibo," *J. Atmos. Sol. Terr. Phys.* **104**, 253–259 (2013).
4. T. Tsuda, X. Chu, T. Nakamura, M. Ejiri, and T. Kawahara, "Sodium layer in the thermosphere (110–130 km) observed at Syowa Station (69.0S, 39.6E) in Antarctica," in *American Geophysical Union (AGU) Fall Meeting*, San Francisco, California, 2012.
5. J. Wang, Y. Yang, X. Cheng, G. Yang, S. Song, and S. Gong, "Double sodium layers observation over Beijing, China," *Geophys. Res. Lett.* **39**, L15801 (2012).
6. X. H. Xue, X. K. Dou, J. Lei, J. S. Chen, Z. H. Ding, T. Li, Q. Gao, W. W. Tang, X. W. Cheng, and K. Wei, "Lower thermospheric-enhanced sodium layers observed at low latitude and possible formation: case studies," *J. Geophys. Res.* **118**, 2409–2418 (2013).
7. X. Chu and G. C. Papen, "Resonance fluorescence lidar for measurements of the middle and upper atmosphere," in *Laser Remote Sensing*, T. Fujii and T. Fukuchi, eds. (CRC Press, 2005), pp. 179–432.
8. W. Grant, E. Browell, R. Menzies, K. Sassen, and C.-Y. She, *Selected Papers on Laser Applications in Remote Sensing* (SPIE, 1997).
9. C. S. Gardner and A. Z. Liu, "Seasonal variations of the vertical fluxes of heat and horizontal momentum in the mesopause region at Starfire Optical Range, New Mexico," *J. Geophys. Res.* **112**, D09113 (2007).
10. C. Y. She, T. Li, R. L. Collins, T. Yuan, B. P. Williams, T. D. Kawahara, J. D. Vance, P. Acott, D. A. Krueger, H.-L. Liu, and M. E. Hagan, "Tidal perturbations and variability in the mesopause region over Fort Collins, CO (41°N, 105°W): continuous multi-day temperature and wind lidar observations," *Geophys. Res. Lett.* **31**, L24111 (2004).
11. T. Yuan, H. Schmidt, C. Y. She, D. Krueger, and S. Reising, "Seasonal variations of semidiurnal tidal perturbations in mesopause region temperature and zonal and meridional winds above Fort Collins, Colorado (40.6°N, 105.1°W)," *J. Geophys. Res.* **113**, D20103 (2008).
12. W. Pan and C. S. Gardner, "Seasonal variations of the atmospheric temperature structure at South Pole," *J. Geophys. Res.* **108**, 4564 (2003).
13. T. D. Kawahara, C. S. Gardner, and A. Nomura, "Observed temperature structure of the atmosphere above Syowa

- Station, Antarctica (69°S, 39°E),” *J. Geophys. Res.* **109**, D12103 (2004).
14. F.-J. Lübken, J. Höffner, T. P. Viehl, B. Kaifler, and R. J. Morris, “First measurements of thermal tides in the summer mesopause region at Antarctic latitudes,” *Geophys. Res. Lett.* **38**, L24806 (2011).
 15. C. Fricke-Begemann and J. Höffner, “Temperature tides and waves near the mesopause from lidar observations at two latitudes,” *J. Geophys. Res.* **110**, D19103 (2005).
 16. J. S. Friedman and X. Chu, “Nocturnal temperature structure in the mesopause region over the Arecibo Observatory (18.35° N, 66.75°W): seasonal variations,” *J. Geophys. Res.* **112**, D14107 (2007).
 17. X. Chu, C. S. Gardner, and S. J. Franke, “Nocturnal thermal structure of the mesosphere and lower thermosphere region at Maui, Hawaii (20.7°N), and Starfire Optical Range, New Mexico (35°N),” *J. Geophys. Res.* **110**, D09S03 (2005).
 18. C. Chen, X. Chu, A. J. McDonald, S. L. Vadas, Z. Yu, W. Fong, and X. Lu, “Inertia-gravity waves in Antarctica: a case study with simultaneous lidar and radar measurements at McMurdo/Scott Base (77.8°S, 166.7°E),” *J. Geophys. Res. Atmos.* **118**, 2794–2808 (2013).
 19. W. Fong, X. Lu, X. Chu, T. J. Fuller-Rowell, Z. Yu, B. R. Roberts, C. Chen, C. S. Gardner, and A. J. McDonald, “Winter temperature tides from 30 to 110 km at McMurdo (77.8°S, 166.7°E), Antarctica: lidar observations and comparisons with WAM,” *J. Geophys. Res. Atmos.* **119**, 2846–2863 (2014).
 20. National Science Foundation, *CEDAR: The New Dimension: Strategic Vision for the National Science Foundation Program on Coupling, Energetics and Dynamics of Atmospheric Regions* (National Science Foundation, 2011).
 21. National Research Council, *Solar and Space Physics: A Science for a Technological Society*, (The National Academies, 2013).
 22. C. S. Gardner, “Sodium resonance fluorescence lidar applications in atmospheric science and astronomy,” *Proc. IEEE* **77**, 408–418 (1989).
 23. C. Yamashita, X. Chu, H.-L. Liu, P. J. Espy, G. J. Nott, and W. Huang, “Stratospheric gravity wave characteristics and seasonal variations observed by lidar at the South Pole and Rothera, Antarctica,” *J. Geophys. Res.* **114**, D12101 (2009).
 24. X. Chu, Z. Yu, C. Chen, W. Fong, W. Huang, C. Gardner, Z. Wang, B. Roberts, and J. A. Smith, “McMurdo lidar campaign: a new look into polar upper atmosphere,” *Proc. ILRC* **26**, 1019–1022 (2012).
 25. W. Huang, X. Chu, B. P. Williams, S. D. Harrell, J. Wiig, and C.-Y. She, “Na double-edge magneto-optic filter for Na lidar profiling of wind and temperature in the lower atmosphere,” *Opt. Lett.* **34**, 199–201 (2009).
 26. W. Huang, X. Chu, J. Wiig, B. Tan, C. Yamashita, T. Yuan, J. Yue, S. D. Harrell, C.-Y. She, B. P. Williams, J. S. Friedman, and R. M. Hardesty, “Field demonstration of simultaneous wind and temperature measurements from 5 to 50 km with a Na double-edge magneto-optic filter in a multi-frequency Doppler lidar,” *Opt. Lett.* **34**, 1552–1554 (2009).
 27. W. Huang, X. Chu, C. S. Gardner, Z. Wang, W. Fong, J. a. Smith, and B. R. Roberts, “Simultaneous, common-volume lidar observations and theoretical studies of correlations among Fe/Na layers and temperatures in the mesosphere and lower thermosphere at Boulder Table Mountain (40°N, 105°W), Colorado,” *J. Geophys. Res. Atmos.* **118**, 8748–8759 (2013).
 28. C. S. Gardner and A. Z. Liu, “Measuring eddy heat, constituent, and momentum fluxes with high-resolution Na and Fe Doppler lidars,” *J. Geophys. Res. Atmos.* **119**, 10583–10603 (2014).
 29. OASIS, “Exploring the interaction of Earth’s atmosphere with space,” Report to NSF, 2014, available at <http://rsss.csl.illinois.edu/workshop>.
 30. G. Megie, F. Bos, J. Blamont, and M. Chanin, “Simultaneous nighttime lidar measurements of atmospheric sodium and potassium,” *Planet. Space Sci.* **26**, 27–35 (1978).
 31. B. Welsh and C. Gardner, “Nonlinear resonant absorption effects on the design of resonance fluorescence lidars and laser guide stars,” *Appl. Opt.* **28**, 4141–4153 (1989).
 32. P. von der Gathen, “Saturation effects in Na lidar temperature measurements,” *J. Geophys. Res.* **96**, 3679–3690 (1991).
 33. P. Milonni, R. Fugate, and J. Telle, “Analysis of measured photon returns from sodium beacons,” *J. Opt. Soc. Am. A* **15**, 217–233 (1998).
 34. P. Milonni, H. Fearn, J. Telle, and R. Fugate, “Theory of continuous-wave excitation of the sodium beacon,” *J. Opt. Soc. Am. A* **16**, 2555–2566 (1999).
 35. M. P. Bristow, “Suppression of afterpulsing in photomultipliers by gating the photocathode,” *Appl. Opt.* **41**, 4975–4987 (2002).
 36. M. P. Bristow, D. H. Bundy, and A. G. Wright, “Signal linearity, gain stability, and gating in photomultipliers: application to differential absorption lidars,” *Appl. Opt.* **34**, 4437–4452 (1995).
 37. A. A. P. Boechat, D. Su, D. R. Hall, and J. D. Jones, “Bend loss in large core multimode optical fiber beam delivery systems,” *Appl. Opt.* **30**, 321–327 (1991).
 38. J. McKay, “Modeling of direct detection Doppler wind lidar. I. The edge technique,” *Appl. Opt.* **37**, 6480–6486 (1998).
 39. B. Liu, F. Yi, and C. M. Yu, “Methods for optical adjustment in lidar systems,” *Appl. Opt.* **44**, 1480–1484 (2005).
 40. R. Wuerker, “Bistatic liquid mirror telescope lidar alignment,” *Opt. Eng.* **36**, 1421–1424 (1997).
 41. F. Chéreau, M. Gates, B. Marinov, A. Wolf, T. Reaves, G. Chéreau, G. Zotti, F. Majerech, J. Müller, M. Cardinot, H. Lambermont, B. Gerdes, and K. AlAjaji, “Stellarium,” 2014, <http://www.stellarium.org/>.
 42. A. Bucholtz, “Rayleigh-scattering calculations for the terrestrial atmosphere,” *Appl. Opt.* **34**, 2765–2773 (1995).
 43. J. Höffner and J. S. Friedman, “The mesospheric metal layer topside: examples of simultaneous metal observations,” *J. Atmos. Sol. Terr. Phys.* **67**, 1226–1237 (2005).
 44. X. Chu, W. Huang, J. S. Friedman, and J. P. Thayer, “MRI: mobile Fe-resonance/Rayleigh/Mie Doppler lidar principle, design, and analysis,” *Proc. ILRC* **24**, 801–804 (2008).
 45. X. Chu, W. Huang, J. P. Thayer, Z. Wang, and J. A. Smith, “Progress in MRI Fe-resonance/Rayleigh/Mie Doppler lidar,” *Proc. ILRC* **25**, 947–950 (2010).
 46. X. Chu and W. Huang, “Fe Doppler-free spectroscopy and optical heterodyne detection for accurate frequency control of Fe-resonance Doppler lidar,” *Proc. ILRC* **25**, 969–972 (2010).
 47. T. Pfrommer, P. Hickson, and C.-Y. She, “A large-aperture sodium fluorescence lidar with very high resolution for mesopause dynamics and adaptive optics studies,” *Geophys. Res. Lett.* **35**, L15831 (2009).